Bedrock fault roughness resolves slip increments of large earthquakes: Case studies from Central Italy

Olaf Zielke, Lucilla Benedetti, Paul Martin Mai, Jules Fleury, Magali Rizza, Sophie Viseur

Bedrock fault roughness resolves slip increments of large earthquakes, case studies from Central Italy

Authors:

Olaf Zielke[1*], Lucilla Benedetti[2], Paul Martin Mai[1], Jules Fleury[2]

Magali Rizza[2], Sophie Viseur[2]

[1]*Physical Science and Engineering Division, King Abdullah University of Science and Technology (KAUST), Building 1, 23955 Thuwal, Saudi Arabia.*

[2]*Centre Européen de Recherche et d'Enseignement en Géosciences de l'Envi, CEREGE, Technopôle de l'Arbois-Méditerranée, BP80, 13545 Aix-Provence, France*

*Corresponding author: **olaf.zielke@kaust.edu.sa**

Abstract

While the cyclic nature of tectonic strain build-up and release is at least conceptually well understood (known as the earthquake cycle), it is not clear how variable the corresponding earthquake sizes and the time intervals between them are. Additional observations from past earthquakes are required to better constrain these aspects.

In this context, we investigate the roughness of bedrock normal fault scarps along the Mt. Vettore fault and Roccapreturo fault (Italy), motivated by field observations that roughness positively correlates with profile height: higher sections of the fault surface are rougher than lower sections, ostensibly because the scarps were created by subsequent exposure events (e.g., earthquakes), exposing the higher sections for longer periods of time to subaerial weathering processes. Using high-resolution topographic models of the two fault surfaces, we calculate local roughness metrics and determine how they change as a function of profile height. In doing so, we are able to identify step-like changes in fault roughness, suggesting that the studied portions of the Mt. Vettore and Roccapreturo fault scarps were formed respectively by at least 6 and 4 large earthquakes, with slip increments ranging from 0.2 m to 1.7 m and corresponding magnitudes ranging from **M**6.1 to **M**6.8. Comparing our results for the Roccapreturo scarp with a previous cosmogenic radionuclide (CRN) investigation at this site indicates that we were able to a) find previously identified earthquakes and b) find additional, previously unresolved ones. Apparently, fault surface roughness may increase at a higher rate than CRNs accumulate over the same time, providing additional fidelity to resolve a bedrock scarp's exposure history.

Introduction

One of the main goals of the active tectonics community is to better resolve the details of the earthquake cycle, which to first order comprises alternating phases of interseismic strain accumulation and coseismic strain release (e.g., Reid, 1910; McCalpin, 2009; Scholz, 2019). Respective studies aim, for example, to determine a fault's geologic slip-rate (variation) and investigate the recurrence of earthquakes that release interseismically accumulated strain, using the tools from paleoseismology and tectonic geomorphology (with augmenting insights from historical accounts of earthquake occurrence and instrumental recordings of the earthquake cycle, as provided by seismic and geodetic data). Paleoseismic studies typically analyze deformed stratigraphic units, exposed via trench excavations, to constrain the time and size of past earthquakes at a specific site along a fault (e.g., Sieh et al., 1989; Grant et al., 1994; Weldon et al., 2004; Zielke and Strecker, 2009; Akciz et al., 2010; Scharer et al., 2014). Tectono-geomorphic studies, on the other hand, commonly analyze tectonically displaced or deformed landforms, such as alluvial fans, river terraces, or channel beds, to constrain a fault's slip-rate and its slip accumulation pattern along larger stretches of a fault (e.g., Wallace, 1968; Sieh, 1978; McCalpin, 2009; Zielke et al., 2010; Klinger et al., 2011). Utilizing these kinds of approaches, a set of end-member models for earthquake recurrence and along-fault slip accumulation was postulated (e.g., Shimazaki and Nakata, 1980; Schwartz and Coppersmith, 1984; Youngs and Coppersmith, 1985; Sieh, 1996) and finds application in seismic hazard assessment. Since then, numerous studies extended on this work and used fault slip and age data, spanning many different time scales (from a few thousands to millions of years), to produce fault growth and earthquake recurrence models that reconcile fault slip accumulation over a range of time scales (e.g., Friedrich et al., 2003; Nicol et al., 2005; Mouslopoulou et al., 2009; Carafa et al., 2022).

While paleoseismic and tectono-geomorphic techniques dominate the tool set that is used to constrain the details of the earthquake cycle, other techniques exist. For example, measuring the concentration of cosmogenic radionuclides (CRNs) along the free face of bedrock fault scarps (for convenience, we will refer to "free faces of bedrock fault scarps" as "fault surfaces" for the remainder of this text) may indicate the time and size of the scarp-forming earthquakes. So far, this approach has been mainly applied on limestone bedrock normal fault scarps, based on the observation that Ca produced ^{36}Cl, an unstable cosmogenic

nuclide, when exposed to cosmic radiation. The concentration of these CRNs is, among other factors, a function of exposure intensity and time (e.g., Dunai, 2010; Schimmelpfennig et al., 2009). Distinct changes in the ^{36}Cl concentration along a fault surface's height may therefore indicate the occurrence of subsequent earthquakes (Fig. 1; e.g., Schlagenhauf et al., 2010; Benedetti et al., 2013; Ren et al., 2018, Tesson and Benedetti, 2019). Another relative dating technique that is aimed at identifying the number of paleoearthquakes on limestone fault surfaces is the REE method. This method measures changes in the geochemistry across a fault surface (identifying the depletion and enrichment of certain elements due to fault surface exhumation and erosion; e.g., Manighetti et al., 2010; Mouslopoulou et al., 2011, 2012). Additional insight is provided by the Schmidt hammer method (Tye and Stahl, 2018; Stahl and Tye, 2020), revealing weathering contrasts in limestone fault scarps via its rebound values (R-values).

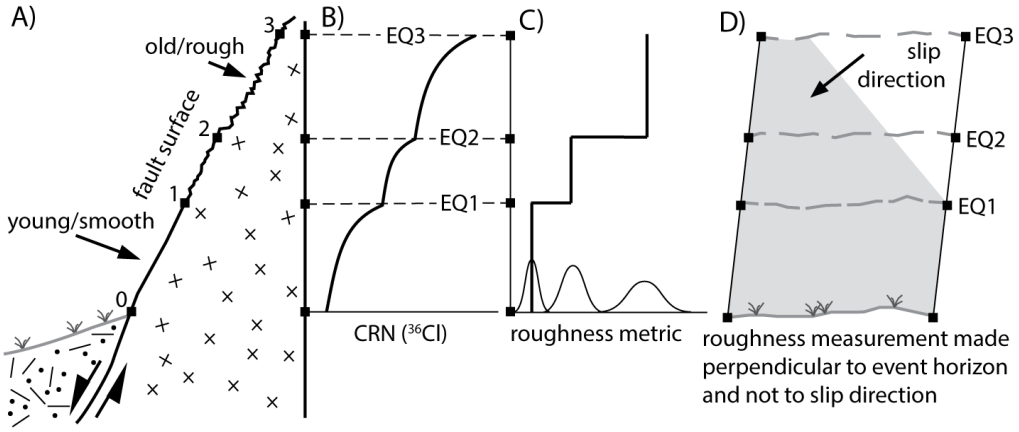

Figure 1. Schematic representation of a normal fault surface, highlighting its roughness and cosmogenic radionuclide CRN concentration as a function of profile height. A) Qualitative observations find that fault surface roughness increases with height. Numbered squares show the height of paleo-earthquake event horizons, indicating where the ground surface of the hanging wall (gray line) touched the footwall at the time of an earthquake. B) CRN concentration profiles may exhibit distinct breaks, indicative for individual exposure events (e.g., earthquakes). C) Similarly, distinct step-like changes in surface roughness along a scarp profile may indicate exposure events. Bell-shaped curves represent the histogram of roughness observations. D) Note that roughness measurements (like CRN measurements) are taken perpendicular to event horizons (indicated by sub-horizontal dashed lines) and not perpendicular to slip direction (black arrow). Doing the latter would mean to mix fault surfaces with different exposure age if the slip vector is distinctly oblique (gray area indicates this for EQ1).

In the present study, we also aim to identify abrupt changes in fault surface exposure time and hence to identify the occurrence of past earthquakes (i.e., their slip increments) along bedrock fault scarps. The approach is motivated by qualitative field observations indicating that fault surface roughness (of exposed normal fault scarps) changes systematically with scarp height. For example, fault surfaces along the Mt. Vettore fault (central Italy) are rougher at higher portions of the fault scarp, relative to its lower portions (Fig. 1A). Similar observations were made previously along various faults and quantitatively documented, utilizing lidar or image-based approaches to measure a fault scarp's surface roughness (e.g., Giaccio et al., 2002; Reicherter et al., 2011; Wei et al., 2013; Bubeck et al., 2015; He et al., 2016; Mechernich et al., 2018; Zou et al., 2020; Corradetti et al., 2021).

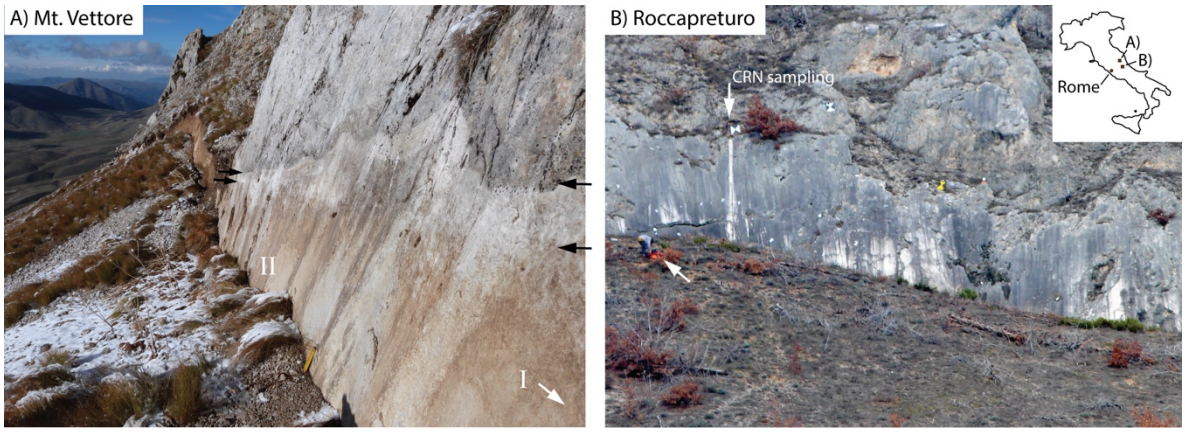

Figure 2. Photographs of the two analyzed fault scarps. A) Imaged here is part II of the Mt. Vettore fault scarp (see Methods section) while part I is located a few meters further to the south (white arrow). Distinct color changes along the scarp (black arrows) reveal the event horizons and hence slip increments of the two most recent earthquakes (August and October 2016, ~0.2 m and ~1.2 m respectively). B) A 10-m long profile was analyzed at the Roccapreturo site for CRN concentrations to determine the age and slip of the scarp-forming earthquakes by Schlagenhauf (2009; white downward-pointing arrow shows sample location). A person is shown for scale in the center left of the image (white arrow). Inset map indicates the location of both study sites with respect to the Italian peninsula and its capital, Rome.

A causal relationship between fault surface roughness and surface age is intuitively plausible, considering that the fault surface is exposed to persistent physical and chemical weathering. The underlying assumption of our study is therefore that prolonged exposure to (subaerial) weathering processes increases the roughness of a fault surface (Fig. 1). Further assuming that

roughness was initially homogeneous across the fault surface may enable us to correlate step-like changes in fault surface roughness to discrete exposure events (e.g., Coradetti et al., 2021). That is, if an initially homogenously rough fault surface is getting exposed sequentially (e.g., due to the occurrence of subsequent earthquakes), then we may find distinct changes in fault roughness perpendicular to the (paleo-) ground surface if a) a sufficient amount of time has passed between subsequent earthquakes to create measurable changes in fault surface roughness, and b) a sufficient amount of slip has occurred during individual earthquakes to produce consistent roughness values along continuous portions of the fault surface (Fig. 1). The assumption of initially homogenous roughness across the fault surface is supported for the Mt. Vettore site, where the newly-exposed fault surface (exposed by the 2016 earthquakes) is indeed homogenously rough, without apparent systematic roughness changes. It is further supported by lithological observations, indicating that the exposed fault surface spans a micritic, compact, and homogeneous Jurassic limestone without observable varying lithologic character (e.g., Pierantoni et al. 2013). Similar observations are made for the Roccapreturo site, where Cretaceous limestone is exposed.

Based on this understanding, we analyze the roughness of bedrock fault surfaces along the Monte Vettore fault and Roccapreturo fault (Fig. 2) to resolve the slip increments of past earthquakes (e.g., Wei et al., 2013; He et al., 2016; Zou et al., 2020). Both faults feature sites with well-developed limestone fault scarps –some of which investigated previously, therefore providing a contextual framework for our own investigation (e.g., Giaccio et al., 2003; Schlagenhauf, 2009; Falcucci et al., 2015; Galli et al., 2019; Coradetti et al., 2021; Goodall et al., 2021). The two faults are located in the central Apennines (Italy), a NW-trending, ~400 km long and ~100 km wide mountain range that undergoes NE-SW extension at a rate of 3-4 mm/yr (D'Agostino, 2014). Extension is accommodated by 10-30 km long normal faults (such as the Mt. Vettore and Roccapreturo faults), arranged in several sub-parallel, segmented fault systems that are located along the ridge belt (Galadini and Galli, 2000; Vai and Martini, 2013). This belt has been the host to many destructive earthquakes over the last millennium (Rovida et al., 2021). The most recent earthquake episode occurred in 2016, when 9 successive shocks (**M**5 to **M**6.5) ruptured several portions of a ~60 km long fault system in less than half a year (e.g., Perouse et al., 2018 and references there in). Prominent surface ruptures, with maximum throws of 80 to 130 cm, were observed along the Mt. Vettore fault after the largest shock of the

158 sequence (**M**6.5) occurred on 30th October 2016 (Civico et al., 2018). Our first study site is
159 located on this fault, near a place called Scoglio del'Aquila, where the 2016 coseismic surface
160 displacement reached its maximum and where the fault surface (i.e., bedrock fault scarp) is
161 particularly well expressed (Fig. 2A). Paleoseismic studies at other locations along the Mt.
162 Vettore fault system revealed that six surface faulting events (including the most recent ones
163 in 2016) occurred within the past 9 kyrs, with an average return period of 1.8+/-0.3 kyr
164 (Galadini and Galli, 2003; Galli et al., 2019). To our knowledge, no incremental slip amount
165 has been attributed to the individual earthquakes, preceding the most recent one(s).
166 The second study site is located along the Roccapreturo fault. This fault belongs to the
167 Middle Aterno fault system, which is composed of several NW-SE trending, ~10-20 km long
168 faults (Galadini and Galli, 2000). A range of morphological features (e.g., triangular facets,
169 channel knickpoints, strong incision and alluvial fan development) along this fault segment
170 indicate the fault's long-term (10^4-10^5 yr) as well as recent (10^3-10^4 yr) tectonic activity. The
171 Quaternary activity of the Roccapreturo fault was shown also by Falcucci et al. (2015) who
172 found early-Pleistocene continental deposits on both sides of the fault, being offset by ~270m.
173 Falcucci et al., (2015) further found paleoseismic evidence for at least two surface rupturing
174 earthquakes since 3.9 to 7.5 kyrs ago, with an accumulated minimum offset of 0.3 m and 1.8
175 m. Additionally, a CRN investigation by Goodall et al. (2021) suggested that the most recent
176 earthquake occurred ~2.6 kyr ago, in agreement with the findings by Falcucci et al. (2015).
177 Following, we describe our data set and analysis approach before presenting our results.
178
179 **Methodology**
180 To quantitatively investigate roughness variations across a fault surface, we adopt the
181 structure-from-motion approach (e.g., Triggs et al., 1999; Lowe, 2004; Brown and Lowe, 2005;
182 Johnson et al., 2014; Corradetti et al., 2017), enabling us to generate very high-resolution
183 surface models by combining a large number of photographs that image the area of interest
184 from many different angles. In total, 271 photos were acquired in November 2016 for the Mt.
185 Vettore site (imaging two separate parts, I and II, of this fault surface) and 213 photos were
186 acquired in 2019 for the Roccapreturo site. Additionally, one portion of the Mt. Vettore fault
187 surface (part I) was also photographed in September 2016 (in-between the August and October
188 earthquakes, 143 photos) and in June 2018 (108 photos). The resulting point clouds, covering

areas of different sizes, contain more than 37 million data points (Mt. Vettore, part I, 11/2016), 46 million data points (Mt. Vettore, part II, 11/2016), 6 million data points (Mt. Vettore, part I, 09/2016), 8 million data points (Mt. Vettore, part I, 06/2018), and 22 million data points (Roccapreturo, 2019). The Mt. Vettore data sets, acquired in November 2016, are publicly available at unavco.org.

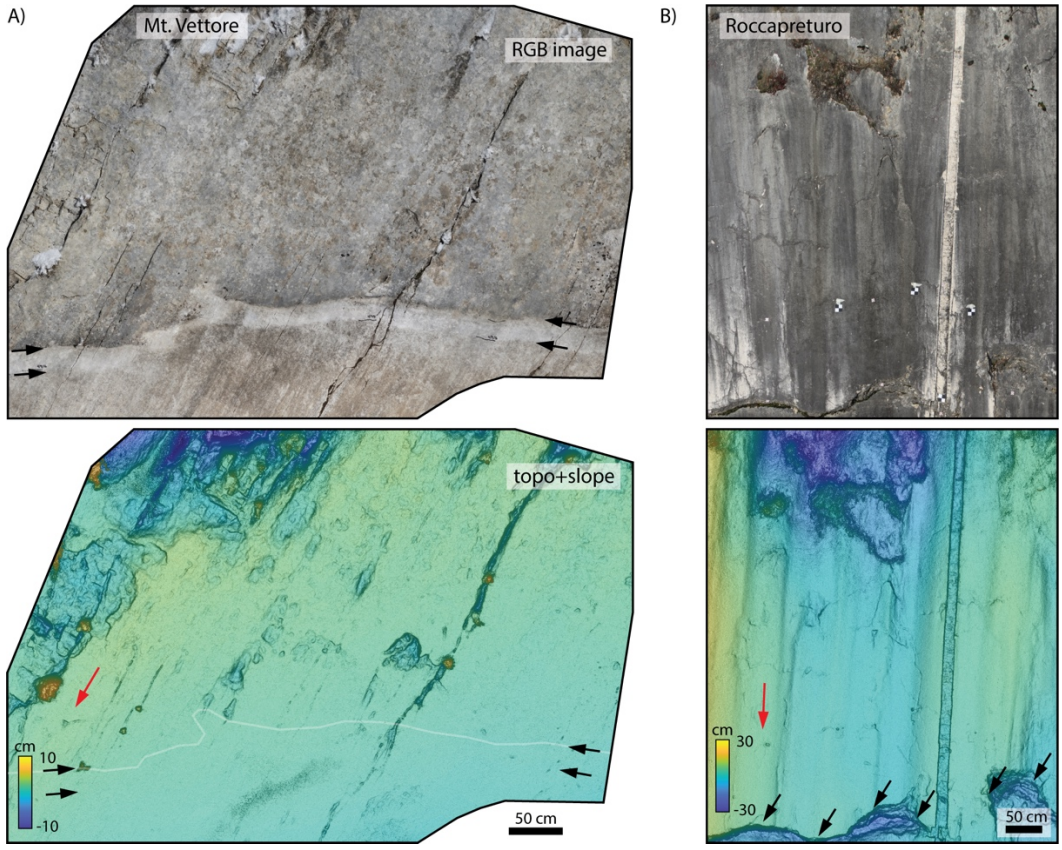

Figure 3. RGB images (top) and combined topography+slope plots (bottom, colors indicate height relative to regression plane) of the investigated fault scarps. Striations across both scarps provide a good indication of respective fault slip direction (red arrows). A) Black arrows indicate the two earthquake event horizons (i.e., the pre-earthquake contact line between hanging wall and footwall) of the August and October 2016 earthquakes. The event horizon of August 2016 earthquake is also shown in the bottom plot (white line). B) The nearly vertical, slot-like feature is due to CRN sampling from Schlagenhauf (2009). Note that the lower portion of the fault surface was dislodged (black arrows indicating trace). The ~1 m high, newly exposed fault surface below this trace is not included in the roughness analysis.

We rotate the point clouds into local coordinate systems where the x-/y-/z-axis correspond to the along-strike-/along-dip-/out-of-plane direction. Next, we linearly interpolate the rotated point clouds to a grid, providing a uniformly spaced data set. We follow Hu et al.'s (2003) suggestion regarding the recommended grid size s which is informed by the data set's average observation point density in the area of interest (observations n per area A) and calculated as $s = sqrt(A/n)$. For all data sets, we have observation point densities in exceedance of 80 cm^{-2}, indicating a permissible grid size of ~1 mm (Fig. 3).

To measure changes in fault surface roughness, we define a circle that is moved across the fault surface in 0.5 cm steps in strike- and dip direction (Fig. 4A). We use circles of three different sizes (2, 4, and 6 cm diameter) to ensure measurements consistency. For each step that the circle is moved across the fault surface, we collect all data points that fall within the circle. Hence, the 2-cm circle contains approximately 300 data points while the 4-cm and 6-cm circles contain ~1,200 and ~2,800 data points respectively. Next, we perform a principal component analysis on this circular subset to remove linear trends from its topography. This step requires for the circle's dimension to be distinctly larger than the topographic signal of the circular subset, indicating the existence of a lower limit for the circle's dimension, relative to the surface's roughness. If this requirement is met, then the first and second principal components define two in-plane coordinate axes, while the third principal component, being perpendicular to the first two, defines the local, detrended topography z of the circular subset.

We measure the circle's roughness by calculating roughness metrics from topography z. In correspondence to choosing different circle sizes, we use three different local roughness metrics (namely the L_2-norm, L_4-norm, and the peak-to-valley method; Gadelmawla et al., 2002; Santos and Julio, 2013) to ensure measurement consistency. The peak-to-valley P2V roughness metric measures the absolute height difference between the highest and lowest point (value of z) within the circular subset, normalized by the circle's diameter D (EQ1; e.g., Gadelmawla et al., 2002). The L_2-norm refers to the common root-mean-square approach for roughness quantification (EQ2; e.g., Power and Tullis, 1991; Santos and Julio, 2013). The L_4-norm (EQ3) differs from the L_2-norm only in the power that is used, making the L_4-norm in principle more sensitive to outliers i.e., more sensitive to roughness variations (Menke, 2012).

226 $$P2V = \frac{1}{D}(z_{max} - z_{min}) \quad (1)$$

227 $$L_2norm = \frac{1}{D}\sqrt{\frac{1}{N}\sum_{i=1}^{N} z_i^2} \quad (2)$$

228 $$L_4norm = \frac{1}{D}\sqrt[4]{\frac{1}{N}\sum_{i=1}^{N} z_i^4} \quad (3)$$

229

230 By moving the circle across the fault surface in small steps (0.5 cm), we typically
231 generate hundreds of roughness measurements for each profile height. Given our assumption
232 that subaerial weathering processes gradually increase fault surface roughness over time, we
233 group the roughness measurements by profile height and then take a low-number percentile to
234 represent the minimum fault roughness at that height (Fig. 4). As a result, we obtain low-
235 roughness vs. height profiles (e.g., 1st and 5th percentile of L_4-norm, Fig. 4B), smoothed with
236 a causal (down-dip looking) moving average filter of 10-cm window size. The smoothed
237 roughness profiles are then normalized to range from 0 to 1, respectively representing its
238 minimum and maximum values. In correspondence to approaches taken in CRN studies, we
239 compute histograms from the smoothed and normalized roughness profiles (Figure 4B, bar
240 plot). Here, histogram peaks indicate profile sections that share the same roughness character
241 while histogram valleys between them indicate profile sections where roughness changes
242 abruptly. The profile heights at which roughness begins to deviate away from the histogram
243 peaks in the up-dip direction constitute event horizons, separating portions of the profile that
244 were exposed to subaerial weathering before and after an exposure event (i.e., surface-rupturing
245 earthquake; Fig. 4B, dashed lines and arrows). To better resolve the event horizons heights,
246 we stack all the roughness profiles we obtained for a given circle size (stacking normalized
247 profiles from different percentile values and roughness metrics) and analyze them collectively,
248 along with the corresponding stacked histogram. This further reduces the data set's noise and
249 helps focusing on signals (e.g., event horizons) that are consistent throughout our observations.
250 Not all parts of the imaged surface represent the initial bedrock fault scarp (i.e.,
251 slickensides) whose degradation by persistent, gradual weathering processes we aim to resolve.
252 Our surface models may contain areas where snow or plants cover the fault surface or where
253 rocks have been plucked and dislodged from it, removing the original slickensides (e.g., upper
254 left part of Fig. 3A, top and bottom part of Fig. 3B). We exclude these non-representative areas

from the roughness analysis by defining polygons that outline the data set sections that we analyze (see auxiliary online material, Fig. S1).

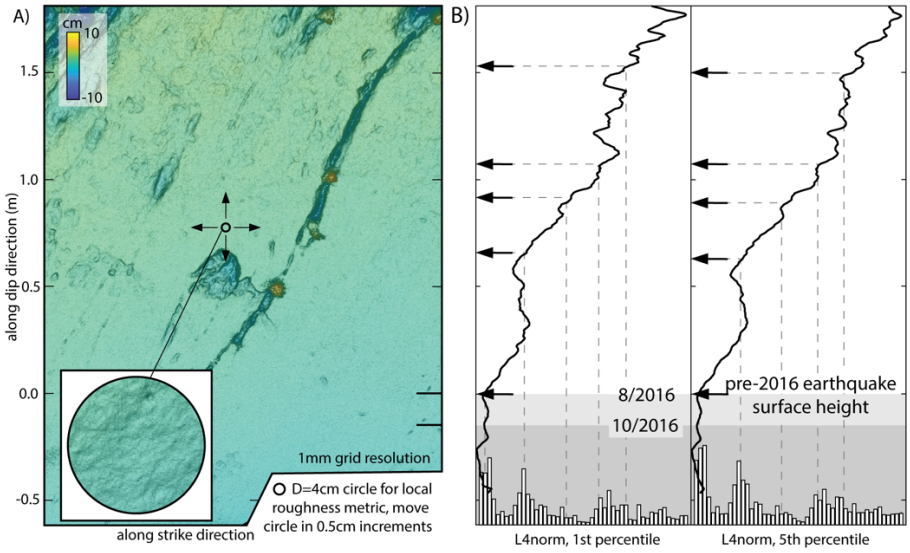

Figure 4. Measurement approach for fault roughness determination. A) A circular sample area is swept across the investigated fault surface. The roughness metric (e.g., L_4-norm) is calculated for each circle position. B) Exemplary, this metric's 1st and 5th percentile are plotted as a function of profile height, smoothed with a 10-cm moving average window (see Methods section). The profile lines and the corresponding histograms indicate which roughness values are more common than others, implicitly revealing profile portions with similar exposure time and the height of event horizons that separate them (black arrows).

Results

Following the outlined approach, we analyze how fault roughness (i.e., its low-percentile representation) changes as a function of profile height at the Mt. Vettore and Roccapreturo sites. In total, we analyzed 5 sections of the fault surface at the Mt. Vettore site and 1 section at the Roccapreturo site. As noted before, three of the Mt. Vettore sections are spatially overlapping, capturing part I of the fault surface (Fig. 3A) at three different times (09/2016, 11/2016, and 06/2018; our measurements on the 09/2016 and 06/2018 data sets may be found in the auxiliary online material; Fig. S2). The other sections are spatially separated, covering different parts of the fault surface as documented by the 11/2016 data set. Performing the analysis on sections that cover different parts of the fault surface (i.e., the same part at different times) further ensures measurement consistency. Unfortunately, we were not able to

take multiple measurements for the Roccapreturo site, where only one fault surface model is available. For each analyzed fault surface section, we provide three subplots (respectively for a 2-, 4-, 6-cm circle size), each of them containing 15 roughness profiles and a stacked roughness histogram (1st to 5th percentile for 3 roughness metrics; Figs. 5 and 6). Profile lines are semi-transparent to emphasize where they share similar values and overlap.

For section 1 of the Mt. Vettore fault surface, we identified five histogram peaks and hence five exposure event horizons (Fig. 5A). Three of them, at 0.0 m, 0.7 m, and 1.5 m, are distinctly larger than the other two at 0.9 m and 1.1 m. The smaller size of the latter two histogram peaks (the one at 0.9 m being the smallest) is due to the short profile sections (~20 cm) that exhibit this roughness character, which makes them presumably less reliable. However, our analysis of section 1, based on the 09/2016 and 08/2018 data sets (Fig. S2), indicates consistency between measurements –even the weakly developed histogram peaks at 0.9 m and 1.1 m are found in the 09/2016 and 06/018 data sets, albeit at slightly shifted heights of 1.0 m and 1.3 m and 0.9 m and 1.2 m respectively (Fig. 5A and S2). This slight shift in height is caused by differences in polygon outlines (Fig. S1), combined with the curviness of the event horizons which is well exemplified for the most recent earthquakes (e.g., Figs. 2A and 3A). Further note that the 09/2016 data set (Fig. S2A) also revealed a histogram peak at 1.8 m, which is not fully resolved in Fig. 5A because of this profile's limited length. The identified event horizon heights, reported relative to height of the August 2016 event horizon, are listed in Table 1.

For section 2 of the Mt. Vettore fault surface (Fig. 5B), we find four well developed histogram peaks, located at 0.0 m, 0.9 m, 1.2 m, and 1.7 m. The changes between profile sections with similar roughness character are overall sharp and discrete (i.e., step-like), especially for the smaller circle sizes (Fig 5B, left and middle). Given the clear expression of the 0.9 m event horizon in section 2 (i.e., its histogram peak), relative to the corresponding one in section 1 (Fig. 5A), leads us to suggests that they are not related to the same exposure event. Instead, we suggest that the 0.9 m event horizon in section 2 correlates to the 0.7 m event horizon in section 1 and further suggest that the 0.9 m event horizon in section 1 is not resolved in section 2 (otherwise, the 0.7 m event horizon from section 1 is not resolved here). Likewise, we suggest that the 1.7 m event horizon in section 2 correlates to the 1.5 m event horizon in section 1.

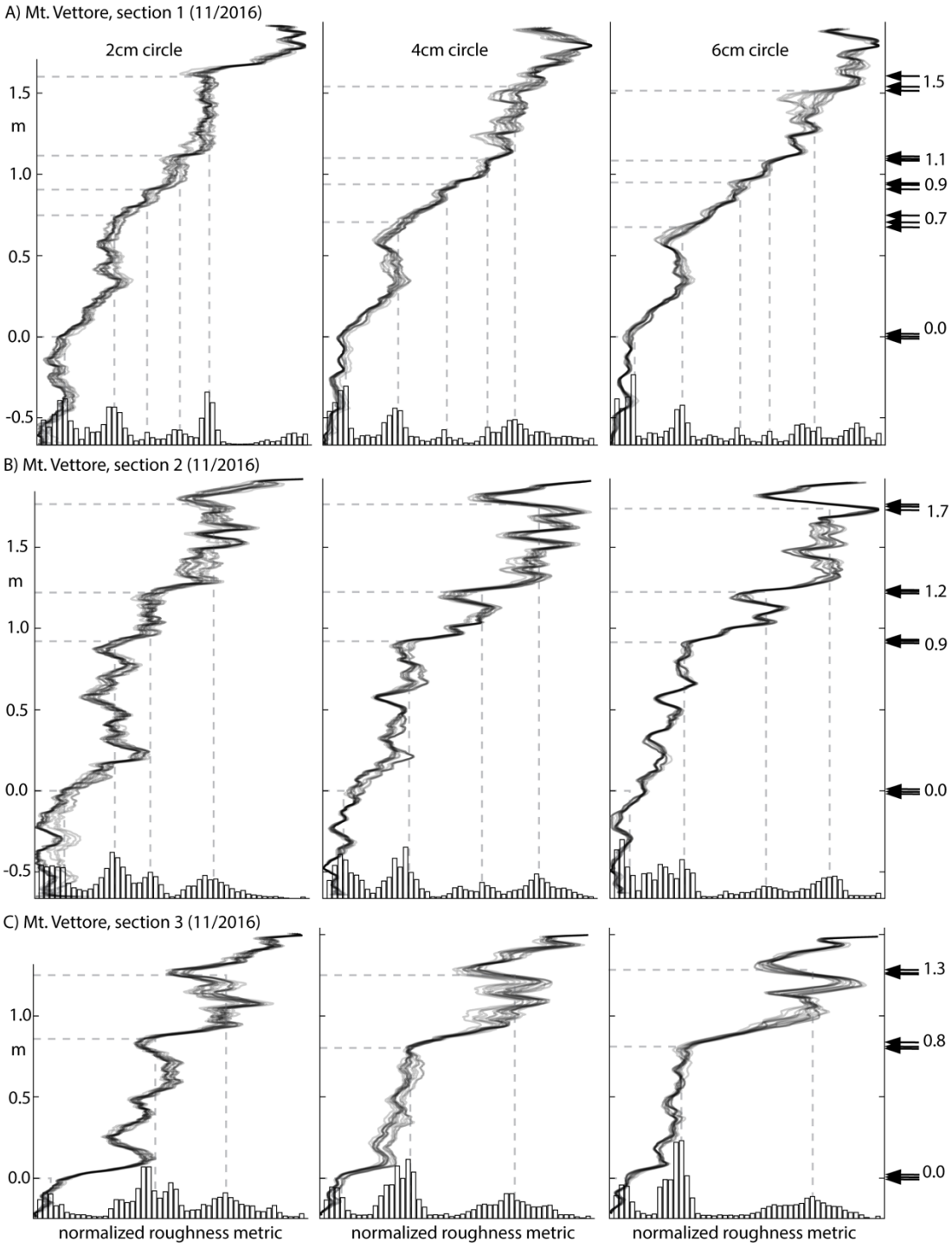

Figure 5. Fault surface roughness as function of profile height for three sections of the Mt. Vettore data set (acquired in 11/2016). See auxiliary online material for section outlines (Fig. S3). Profile heights are relative to the August 2016 event horizon (Fig. 3A). Each subplot contains 15 smoothed and normalized roughness profiles and a stacked roughness histogram (see Methods sections). Dashed lines and black arrows indicate histogram peaks and the corresponding event horizon height.

For section 3 of the Mt. Vettore fault surface (Fig. 5C), we find three well developed histogram peaks, located at 0.0 m, 0.8 m, and 1.3 m, separated by sharp and step-like changes in roughness. Note that this profile is ~0.5 m shorter than those of section 1 and 2, therefore not capturing the higher event horizon at 1.5 m (i.e., 1.7 m). Following the same approach as for section 2 (based on relative expression of the step-like change in roughness and size of the associated histogram peak), we suggest that the 0.8 m event horizon in section 3 correlates to the 0.7 m event horizon in section 1.

Mt. Vettore site	event horizon height (m) section 1 (11/2016)	event horizon height (m) section 1 (09/2016)	event horizon height (m) section 1 (06/2018)	event horizon height (m) section 2 (11/2016)	event horizon height (m) section 3 (11/2016)	Average height of event horizon (m)	Apparent slip increment (m)
EQ 1	0.0	0.0	0.0	0.0	0.0	0.0	0.2, 1.2
EQ 2	0.7	0.7	0.6	0.9	0.8	0.7	0.7
EQ3	*0.9*	*1.0*	*0.9*	-	-	0.9	(0.2)
EQ4	*1.1*	*1.3*	*1.2*	1.2	1.3	1.2	0.5 (0.3)
EQ 5	1.5	1.6	-	1.7	-	1.6	0.4
EQ 6	-	1.8	-		-	1.8	0.2

Table 1. Identified event horizon heights (meters) and corresponding earthquake as derived for the different fault surface sections of the Mt. Vettore site. Italic font indicates weakly expressed event horizons. Also shown are the average heights of event horizons and apparent slip increments. The reported slip increments for EQ1 (the August and October 2016 earthquakes) are from the literature (e.g., Perouse et al., 2018).

Overall, we find that the event horizon heights for the Mt. Vettore site (Table 1) are markedly similar across the different roughness metrics, percentile values, circle sizes, and analyzed fault surface sections, attesting for the consistency of these measurements. Including the 2016 earthquake sequence, we identified 6 exposure event horizons, respectively at 0.0 m, 0.7 m, 0.9 m, 1.2 m, 1.6 m, and 1.8 m profile height (relative to the 08/2016 event horizon height). Assuming that these event horizons represent individual earthquakes, the

corresponding slip increments range from 0.2 m to 1.2 m (Table 1). That said, we want to note that a direct correlation between exposure events, as identified from distinct changes in roughness metric, and individual earthquakes is likely not permissible. Multiple surface rupturing earthquakes may contribute to a single exposure event if these earthquakes occurred shortly after one another, in which case it is better to attribute event horizons to phases of substantial fault activity (potentially encompassing multiple surface ruptures). We will address this point in more detail in the following section.

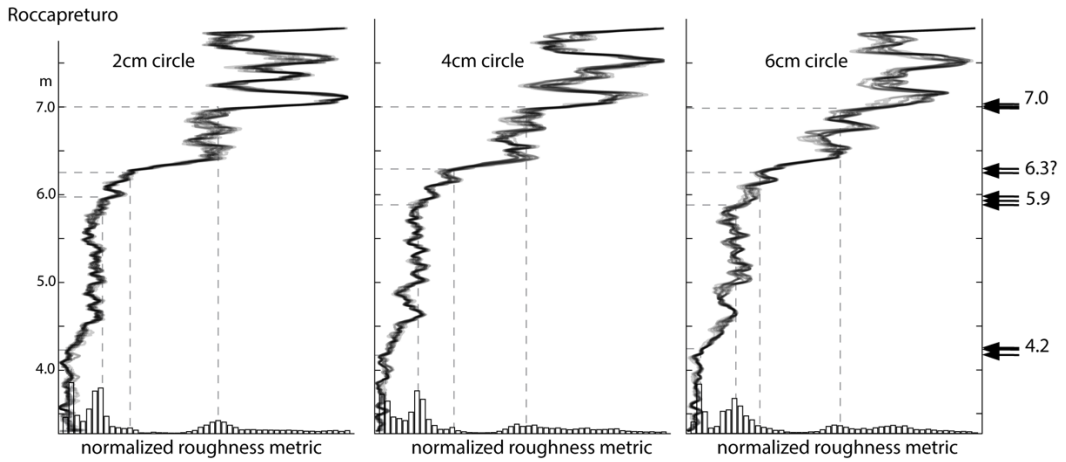

Figure 6. Fault surface roughness as function of profile height for the Roccapreturo data set. See auxiliary online material for section outline (Fig. S4). Profile heights are relative to the base of a 10-m spanning CRN analysis profile (Schlagenhauf, 2009; Fig. 3B). Each subplot contains 15 smoothed and normalized roughness profiles and a stacked roughness histogram (see Methods sections). Dashed lines and black arrows indicate histogram peaks and the corresponding event horizon height.

While positioned along another fault, our findings for the Roccapreturo site are broadly consistent with our findings for Mt. Vettore site (Fig. 6): Fault roughness and its variability increases with profile height, exhibiting profile portions of similar roughness that are separated by sharp, step-like roughness changes. For the Roccapreturo site, we find 3 well developed histogram peaks (i.e., event horizons) at 4.2 m, 5.9 m, and 7.0 m as well as 1 weakly developed peak at 6.3 m. The latter peak is more apparent in the roughness profiles from which the histograms are derived –the corresponding profile section being bracketed by sharp changes in roughness metric (Fig. 6). Overall, the identified histogram peaks are separated by distinct valleys in the roughness histogram, indicative of sharp, step-like changes in roughness metric

when moving from one histogram peak to the next (i.e., moving from one exposure event to the next). Hence, we identified 4 exposure events for the Roccapreturo site with slip increments ranging from 0.4 m to 1.7 m (Table 2). Conveniently, the Roccapreturo site was also the location of a CRN investigation that aimed to determine the exposure history of this fault scarp. This investigation identified event horizons at ~4.4 m and ~7.1 m, with corresponding ages of 2.9 kyrs and 4.5 kyrs (Schlagenhauf, 2009). Our roughness analysis is therefore able to recover these events (EQ1 and EQ4; Table 1; Fig. 6) and presumably able to resolve additional events that were not found in the CRN analysis (at 5.9 m and 6.3 m profile height), highlighting the added value that may come from the roughness analysis. Apparently, the fault surface roughened more quickly than cosmogenic radionuclides accumulated, therefore enabling to resolve smaller variations thereof. Because of lacking data overlap, we were not able to correlate our findings to the paleoseismic study by Falcucci et al. (2015) or the CRN study by Goodall et al., (2021) that were also conducted along the Roccapreturo fault.

Roccapreturo	section 1 (2019)	Apparent slip increment (m)
EQ 1	4.2	-
EQ 2	5.9	1.7
EQ 3	*6.3*	(0.4)
EQ 4	7.0	1.1 (0.7)

Table 2. Identified event horizon heights (meters) and corresponding earthquake number as derived for the different fault surface sections of the Roccapreturo site. Italic numbers indicate weakly expressed event horizons. Also shown are the average heights of event horizons and apparent slip increments. If EQ3 does not represent a separate exposure event, then its slip increment would be accommodated by EQ4 (bracketed values indicate case where EQ3 is assumed to be an exposure event).

Discussion

Our investigation along the Mt. Vettore and Roccapreturo bedrock fault scarps indicates that fault surface roughness changes systematically along profile height, alternating between a) profile sections with similar roughness characteristics and b) approximately step-like changes in roughness over short profile sections. We suggest that these step-like roughness

changes constitute event horizons, separating profile sections that were exposed to subaerial weathering processes for different time periods. In our analysis, we were able to identify 6 event horizons for the Mt. Vettore site and 4 event horizons for the Roccapreturo site, respectively spanning a combined profile height of 3.2 m and 2.8 m (for the Mt. Vettore site, this includes the 2016 earthquakes). Intuitively, we may assume a direct correlation between these event horizons and individual earthquakes. However, this correlation is not sensible as is indicated by observational evidence and was noted before. For example, for the Mt. Vettore site, we know that the ~1.4 m offset from 2016 (EQ1 in Table 1; Fig. 2A) contains the slip contribution of two successive events (August 2016 earthquake with ~0.2 m and October 2016 earthquake with ~1.2 m of slip at the site; Perouse et al., 2018). The slip amount of the August 2016 earthquake and importantly the time interval between these two earthquakes (~3 month) is small, prohibiting to distinguish these events through surface roughness analysis. Hence, the reported histogram peaks and event horizons should not be correlated to individual earthquakes but rather to phases of substantial fault activity, potentially spanning more than one surface-rupturing earthquake. The reported offset increments (Tables 1 and 2) therefore represent the combined slip amount of these phases, potentially containing slip contributions from more than one earthquake (e.g., Grant Ludwig et al., 2010) as is also inferred for the record obtained from the ^{36}Cl exposure dating (Beck et al., 2018, Tesson and Benedetti, 2019).

This understanding raises the question how many earthquakes contributed to each offset increment (i.e., activity phase) that we identified and how variable their respective offsets are. Unfortunately, we are not able to answer this question because we are lacking the necessary observational data (e.g., knowing the event horizon ages to correlated them with paleoseismic studies; e.g., Galli et al., 2019). That said, earthquake physics, rupture simulations, and observational constraints suggest that slip accumulation along faults is dominated by large, full-rupture earthquakes (e.g., Schwartz and Coppersmith, 1984; Youngs and Coppersmith, 1985; Pacheco et al., 1992; Sieh, 1996; Manighetti et al., 2005; Zielke and Arrowsmith, 2008; Akciz et al., 2010; Schlagenhauf et al., 2011; Zielke et al., 2015). With this conceptual framework, we can provide a lower-bound estimate for the number of earthquakes that contributed to fault scarp formation (i.e., the portions we analyzed here) while further assuming that other (non-tectonic) mechanisms that may expose a fault surface can be neglected (e.g., Giaccio et al., 2002; Wiatr et al., 2015; Mechernich et al., 2018). That is, the 3.2-m high scarp

399 at the Mt. Vettore site was formed by at least 6 surface-rupturing earthquakes, with maximum
400 offsets ranging from 0.2 m to 1.2 m. If these offsets are indeed due to the occurrence of a single
401 earthquake, then the corresponding magnitudes would range from **M**6.1 to **M**6.7 (Manighetti
402 et al., 2007; Thingbaijam et al., 2017) –plausible values in comparison to the 2016 earthquake
403 sequence. Likewise, if the offset increments at the Roccapreturo site (ranging from 0.4 to 1.7
404 m) are caused by the occurrence of single, full-rupture earthquakes, then the corresponding
405 magnitudes would range from **M**6.3 to **M**6.8. Note that these magnitude estimates for the Mt.
406 Vettore and Roccpreturo faults are consistent with rupture length to average slip scaling
407 relationships, implying corresponding rupture lengths of 20 to 30 km –comparable to the
408 reported length of these faults systems (Manighetti et al., 2007; Thingbaijam et al., 2017).
409 Going one step further with this line of thinking, we might correlate the 6 event horizons
410 that we identified for the Mt. Vettore scarp (spanning 3.2 m of fault scarp) with the 6 surface-
411 rupturing earthquakes that occurred within the last 9 kyrs along the Mt. Vettore fault (Galli et
412 al., 2019), implying a throw-rate of ~0.3 mm/yr. This rate is consistent with the minimum rate
413 of 0.26-0.38 mm/yr as derived from a single splay fault of a wide zone of deformation (Galli
414 et al., 2019; Cinti et al., 2019; Pucci et al., 2021). However, it is distinctly lower than the fault's
415 long-term rate of 0.7-1.6 mm/yr (Pizzi et al., 2002; Puliti et al., 2020), indicating that either a)
416 the throw-rate slowed down over time, b) the 3.2-m high scarp we investigated was formed by
417 less than 6 earthquakes, c) more than 6 surface-rupturing earthquakes occurred during the last
418 9 kyrs, or d) a combination of these possibilities. To begin resolving this discrepancy, we would
419 first need to know how old the event horizons (from our roughness analysis) are.
420 The Roccapreturo site gives us the opportunity to validate our analysis by comparing it
421 to a previous CRN investigation along this scarp (Schlagenhauf, 2009). We were able to
422 reproduce these earlier findings and further to identify additional surface-rupturing events,
423 implying that fault roughness measurements, under the right conditions, may provide a higher
424 resolution of bedrock scarp exposure events. It appears that fault roughness may change more
425 quickly than CRN can accumulate and hence enable to identify and resolve smaller changes in
426 surface exposure time. However, as noted before, one important missing aspect when it comes
427 to constraining the slip accumulation history at these two sites by solely using roughness
428 measurements is to determine the age of the identified exposure events. At this time, we do not
429 know when these events occurred. Incorporating CRN analysis along these fault scarps to

determine the exposure ages directly above the identified event horizons would improve our understanding, as was possible for the Roccapreturo site. However, defining these ages directly from our roughness measurements requires a) to quantify the relative importance of all acting physical and chemical weathering processes that are responsible for roughness modification, and b) to determine their respective rates, along with the parameters that control them. While this endeavor is beyond the scope of the present study, we anticipate extending in this direction.

Conclusion

In the present study, we analyze high-resolution surface models of exposed fault surfaces from two sites along two faults in Central Italy to determine how fault roughness varies as function of profile height and if it can be used to resolve slip increments of successive earthquakes. In doing so, we can identify 6 and 4 event horizons, respectively spanning a combined height of 3.2 m and 2.8 m for the Mt. Vettore and Roccapreturo site. Making the simplifying assumption that the corresponding slip increments, ranging from 0.2 to 1.7m, were caused by individual subsequent surface-rupturing earthquakes, suggests the repeated occurrence of **M**6.1 to **M**6.8 earthquakes along these faults.

Our findings indicate that, under the right conditions, fault roughness measurements along exposed fault surface provide the means to identify event horizons of fault exposure, indicating distinct phases of fault activity. This analysis approach likely performs better for slow-moving faults, providing more time in between successive earthquakes to form and increase fault surface roughness. We suggest that a combination of surface roughness analysis, as we performed it here (to identify event horizons), and CRN analysis (to assign an age to these event horizons) may further improve our ability to resolve details of the earthquake cycle along bedrock fault scarps.

Acknowledgements

This research project is supported with funding from King Abdullah University of Science and Technology (KAUST), Grant BAS/1/1339-01-01.

Data Availability

460 The point cloud data for the Mt. Vettore site may be found at
461 https://tls.unavco.org/projects/U-067/PS01/SV02/. Other data are contained in this manuscript
462 and the auxiliary online material.
463
464 **Appendices**
465 The auxiliary online material contains two additional figures that a) show the sampling
466 locations for the Mt. Vettore and Roccapreturo sites and b) additional results from the Mt.
467 Vettore site, section 1 (results from the « in-between » data set of 09/2016 and from two years
468 after the 2016 earthquake sequence).
469
470 **References**
471
472 Akçiz, S.O., Grant Ludwig, L., Arrowsmith, J.R., Zielke, O., 2010. Century-long average time
473 intervals between earthquake ruptures of the San Andreas Fault in the Carrizo Plain, California.
474 *Geology* **38**(9), 787–790. http://dx.doi.org/10.1130/G30995.1.
475
476 Beck, J., Wolfers, S., Roberts, G. P., 2018. Bayesian earthquake dating and seismic hazard
477 assessment using chlorine-36 measurements (BED v1). *Geoscientific Model Development*,
478 **11**(11), 4,383-4,397.
479
480 Benedetti, L., Manighetti, I., Gaudemer, Y., Finkel, R., Malavieille, J., Pou, K., Arnold, M.,
481 Aumaitre, G., Bourles, D., Keddadouche, K., 2013. Earthquake synchrony and clustering on
482 Fucino faults (Central Italy) as revealed from in situ ^{36}Cl exposure dating. *J. Geophys. Res.*
483 **118**, 4,948-4,974. http://dx.doi.org/10.1002/jgrb.50299.
484
485 Brown, M., Lowe, D.G., 2005. Unsupervised 3d object recognition and reconstruction in
486 unordered datasets. *Proceedings of the fifth international conference on 3-D digital imaging*
487 *and modeling*, 56-63.
488
489 Bubeck, A., Wilkinson, M., Roberts, G.P., Cowie, P.A., McCaffrey, K.J.W., Phillips, R.,
490 Sammonds, P., 2015. The tectonic geomorphology of bedrock scarps on active normal faults
491 in the Italian Apennines mapped using combined ground penetrating radar and terrestrial laser
492 scanning. *Geomorphology* **237**, 38-51.
493
494 Carafa, M. M. C., Di Naccio, D., Di Lorenzo, C., Kastelic, V., Bird, P., 2022. A meta-analysis
495 of fault slip rates across the central Apennines. *J. Geophys. Res.* **127**, e2021JB023252.
496

Cinti, F.R., DeMartini, P.M., Pantosti, D., Baize, S., Smedile, A., Villani, F., Civico, R., Pucci, S.,
Lombardi, A.M., Sapia, V., Pizzimenti, L., Caciagli, M., Brunori, C.A., 2019. 22-kyr-long record of surface faulting along the source of the 30 October 2016 earthquake (Central Apennines, Italy), from integrated paleoseismic data sets. J. Geophys. Res. Solid Earth 124 (8), 9021–9048. https://doi.org/10.1029/2019JB017757

Corradetti, A., McCaffrey, K.J.W., De Paola, N., and Tavani, S., 2017. Evaluating roughness scaling properties of natural active fault surfaces by means of multi-view photogrammetry: *Tectonophysics* **717**, 599–606.

Corradetti, A., Zambrano,M., Tavani, S., Tondi, E., Seers, T.D., 2021. The impact of weathering upon the roughness characteristics of a splay of the active fault system responsible for the massive 2016 seismic sequence of the Central Apennines, Italy. *Geol. Soc. Am. Bull.* **133**, 885-896.

Civico, R., Pucci, S., Villani, F., Pizimenti, L., De Martini, P.M., Nappi, R., 2018. Surface ruptures following the 30 October 2016 Mw6.5 Norcia earthquake, Central Italy. *Journal of Maps* **14**(2), 151-160.

D'Agostino, N., 2014. Complete seismic release of tectonic strain and the earthquake recurrence in the Apennines (Italy). *Geophys. Res. Lett.* **41**(4), 1,155-1,162.

Dunai, T.J. 2010. Cosmogenic nuclides: Principles, concepts and applications in the earth surface sciences. Cambridge University Press, U.K.

Falcucci, E., Gori, S., Moro, M., Fubelli, G., Saroli, M., Chiarabba, C., Galadini, F., 2015. Deep reaching versus vertically restricted quaternary normal faults: Implications on seismic potential assessment in tectonically active regions: Lessons from the middle Aterno valley fault system, central Italy. *Tectonophysics* **651**, 186-198.

Friedrich, A., Wernicke, B.P., Niemi, N.A., Bennett, R.A., Davis, J.L., 2003. Comparison of geodetic and geologic data from the Wasatch region, Utah, and implications for the spectral character of Earth deformation at periods of 10 to 10 million years. *J. Geophys. Res.* **108**, 2199.

Gadelmawla, E.S., Koura, M.M., Maksoud, T.M.A., Elewa, I.M., Soliman, H.H., 2002. Roughness parameters. *J. Mat. Proc. Tech.* **123**, 133-145.

Galadini, F., Galli, P., 2000. Active tectonics in the central Apennines (Italy) -Input data for seismic hazard assessment. *Natural Hazards* **22**(3), 225-268.

538 Galladini, F., Galli, P., 2003. Paleoseismology of silent faults in the central Apennines (Italy):
539 The Mt. Vettore and Laga Mts. Faults. *Annals of Geophys*. **46**, 815-836.
540 Galli, P., Galderisi, A., Peronace, E., Giaccio, B., Hajdas, I., Messina, P., Pileggi, D., Poletta,
541 F., 2019. The awakening of the dormant Mount Vettore Fault (2016 central Italy earthquake,
542 Mw 6.6): Paleoseismic clues on its millennial silences. *Tectonics* **38**, 687-705.
543
544 Giaccio, B., Galadini, F., Sposato, A., Messina, P., Moro, M., Zreda, M., Cittadini, A., Salvi,
545 S., Todero, A., 2002. Image processing and roughness analysis of exposed bedrock fault planes
546 as a tool for paleoseismological analysis: results from the Campo Felice fault (central
547 Apennines, Italiy). *Geomorphology* **49**, 281-301.
548
549 Goodall, H.J., Gregory, L.C., Wedmore, L.N.J., McCaffrey, K.J.W., Amey, R.M.J., Roberts,
550 G.P., Shanks, R.P., Phillips, R.J., Hooper, A., 2021. Determining histories of slip on normal
551 faults with bedrock scarps using cosmogenic nuclide exposure data. *Tectonics* **40**
552 http://dx.doi.org/10.1029/2020TC006457.
553
554 Grant, L.G., Sieh, K.E., 1994. Paleoseismic evidence of clustered earthquakes on the San
555 Andreas fault in the Carrizo Plain, California. *J. Geophys. Res.* **99**(4), 6,819-6,841.
556
557 Grant-Ludwig, L.G., Akciz, S.O., Noriega, G.R., Zielke, O., Arrowsmith, J R., 2010. Climate-
558 modulated channel incision and rupture history of the San Andreas Fault in the Carrizo Plain.
559 *Science* **327**, 1117.
560
561 He, H., Wei, Z., Densmore, A., 2016. Quantitative morphology of bedrock fault surfaces and
562 identification of paleo-earthquakes. *Tectonophysics* **693**, 22-31.
563 http:dx.doi.org/10.1016/j.tecto.2016.09.032.
564
565 Hu, Y., 2003. Automated extraction of digital terrain models, roads and buildings using
566 airborne lidar data. Department of Geomatics Engineering, University of Calgary, Canada
567 (PhD dissertation).
568
569 Johnson, K., Nissen, E., Saripalli, S., Arrowsmith, J.R., McGarey, P., Scharer, K., Williams,
570 P., Blisniuk, K., 2014. Rapid mapping of ultra-fine fault zone topography with structure from
571 motion. *Geosphere* **10**(5), 1-18. http://dx.doi.org/10.1130/GES01017.1.
572
573 Klinger, Y., Etchebes, M., Tapponier, P., Narteau, C., 2011. Characteristic slip for five great
574 earthquakes along the Fuyun fault in China. *Nat. Geosci.* **4**, 389-392.
575 http://dx.doi.org/10.1038/NGEO1158.
576

Lowe, D.G., 2004. Distinctive image features from scale-invariant keypoints. *Int. J. Comput. Vision* **60**(2), 91-110.

Manighetti, I., Campillo, M., Sammis, C., Mai, P. M., King, G., 2005. Evidence for self-similar, triangular slip distributions on earthquakes: Implications for earthquake and fault mechanics. *J. Geophys. Res.* **110**(5). B05302. http://dx.doi.org/10.1029/2004JB003174.

Manighetti, I., Campillo, M., Bouley, S., Cotton, F., 2007. Earthquake scaling, fault segmentation, and structural maturity. *Earth and Planet. Sci. Lett.* **253**, 429-438.

Manighetti, I., Boucher, E., Chauvel, C., Schlagenhauf, A., Benedetti L., 2010. Rare earth elements record past earthquakes on exhumed limestone fault planes. *Terra Nova* **22**, 477-482.

McCalpin, J.P., 2009. *Paleoseismology*. 2nd edition. Academic Press, San Diego, CA.

Mechernich, S., Schneiderwind, S., Mason, J., Papanikolaou, I.D., Deligiannakis, G., Pallikarakis, A., Binnie, S.A., Dunai, T.J., Reicherter, K., 2018. The seismic history of the Pisia fault (eastern Corinth rift, Greece) from fault plane weathering features and cosmogenic ^{36}Cl dating. *J. Geophys. Res.* **123**, 4,266-4,284.

Menke, W., 2012. *Geophysical data analysis: Discrete inverse theory, MATLAB edition*. 3rd edition, Academic Press, San Diego, CA.

Mouslopoulou, V., Walsh, J.J., Nicol, A., 2009. Fault displacement rates on a range of timescales. *Earth and Planet. Sci. Lett.* **278**, 186-197.

Mouslopoulou, V., Moraetis, D., Fassoulas, C., 2011. Identifying past earthquakes on carbonate faults: advances and limitations of the Rare Earth Element method based on analysis of the Spili Fault, Crete, Greece. *Earth and Planet. Sci. Lett.* **309**, 45-55.

Mouslopoulou, V., Nicol, A., Walsh, J.J., Begg, J.G., Townsend, D.B., Hristopulos, D.T., 2012. Fault-slip accumulation in an active rift over thousands to millions of years and the importance of paleoearthquake sampling. *J. Struct. Geol.* **36**, 71-80.

Nicol, A., Walsh, J.J., Berryman, K., Nodder, S., 2005. Growth of a normal fault by the accumulation of slip over millions of years. *J. Struct. Geol.* **27**, 327-342.

Pacheco, J.F., Scholz, C.H., Sykes, L.R., 1992. Changes in frequency-size relationship from small to large earthquakes. *Nature* **355**, 71-73.

Perouse, E., Benedetti, L., Fleury, J., Rizza, M., Puliti, I., Billant, J., Van der Woerd, J., Feuillet, N., Jacques, E., Pace, B., 2018. Coseismic slip vectors of 24 August and 30 October 2016

earthquakes in Central Italy: Oblique slip and regional kinematic implications. *Tectonics* **37**(10), 3,760-3,781.

Pierantoni, P. P., Deiana, G., & Galdenzi, S., 2013. Stratigraphic and structural features of the Sibillini Mountains (Umbria–Marche Apennines, Italy). *Italian J. of Geosciences* **132**, 497–520. https://doi.org/10.3301/IJG.2013.08.

Pizzi, A., Calamita, F., Coltorti, M., & Pieruccini, P., 2002). Quaternary normal faults, intramontane basins and seismicity in the Umbria-Marche-Abruzzi Apennine ridge (Italy): Contribution of neotectonic analysis to seismic hazard assessment. Bollettino Della Società Geologica Italiana, 1, 923–929.

Power, W.L., Tullis, T.E., 1991. Euclidean and fractal models for the description of rock surface roughness. *J. Geophys. Res.* **96**(1), 415-424.

Pucci, S., Pizzimenti, L., Civico, R., Villani, F., Brunori, C.A., Pantosi, D., 2021. High resolution morphometric analysis of the Cordone del Vettore normal fault scarp (2016 central Italy seismic sequence): insights into age, earthquake recurrence and throw rates. Geomorphology 388, 107784.

Puliti, I., Pizzi, A., Benedetti, L., DiDomenica, A., Fleury, J., 2020. Comparing slip distribution of an active fault system at various time scales: Insights for the evolution of the Mt. Vettore-Mt. Bove fault system in central Apennines. *Tectonics* **39**, 1-22,

Reicherter, K., Hoffmann, N., Lindhorst, K., Krastel, S. , Fernández-Steeger, T., Grützner, C. and Wiatr, T., 2011. Active basins and neotectonics: morphotectonics of the Lake Ohrid Basin (FYROM and Albania). *Zeitschrift der Deutschen Gesellschaft für Geowissenschaften* **162**.

Reid, H.F., 1910. The California Earthquake of April 18, 1906 (edited by Washington, C. I. o.). *Report of the State Earthquake Investigation Commission* **Volume II, The Mechanics of the Earthquake**, Washington, D.C., 190pp.

Ren, Z., Zielke, O., Yu, J., 2018. Active tectonics in 4D high-resolution. *J. Struct. Geol.* **117**, 264-271. http://dx.doi.org/10.1016/j.jsg.2018.09.015.

Rovida, A.N., Locati, M., Camassi, R.D., Lolli, B., Gasperini, P., 2021. Catalogo Parametrico dei Terremoti Italiani (CPTI15), versione 3.0. Istituto Nazionale di Geofisica e Vulcanologia (INGV). https://doi.org/10.13127/CPTI/CPTI15.3.

Santos, P.M.D., Júlio, E.N.B.S., 2013. A state-of-the-art review on roughness quantification methods for concrete surfaces. *Const. Build. Mat.* **38**, 912-923. http://dx.doi.org/10.1016/j.conbuildmat.2012.09.045.

Scharer, K., Weldon II, R., Streig, A., Fumal, T., 2014. Paleoearthquakes at Frazier Mountain, California delimit extent and frequency of past San Andreas Fault earthquakes along 1857 trace. *Geophys. Res. Lett.* **41**, 4,527-4,534. http://dx.doi.org/10.1002/2014GL060318.

Schimmelpfennig, I., Benedetti, L., Finkel, R., Pik, R., Blard, P. H., Bourles, D., Burnard, P., Williams, A., 2009. Sources of in-situ 36Cl in basaltic rocks. Implications for calibration of production rates. *Quaternary Geochronology* **4**(6), 441-461.

Schlagenhauf, A., 2009. Identification des forts séismes passes sur les failles normales actives de la region Lazio-Abruzzo (Italie Centrale) par 'datations cosmogéniques' (^{36}Cl) de leurs escarpements. Thesis, Univ. J. Fourier, Grenoble, France, pp300

Schlagenhauf, A., Gaudemer, Y., Benedetti, L. Manighetti, I., Palumbo, L., Schimmelpfenning, I., Finkel, R., Pou, K., 2010. Using in situ chlorine-36 cosmonuclide to recover past earthquake histories on limestone normal fault scarps: A reappraisal of methodology and interpretations. *Geophys. J. Int.* **182**(1), 36. http://dx.doi.org/10.1111/j.1365-246X.2010.04622.x.

Schlagenhauf, A., Manighetti, I., Benedetti, L., Gaudemer, Y., Finkel, R., Malavieille, J., Pou, K., 2011. Earthquake supercycles in Central Italy, inferred from 36Cl exposure dating. *Earth and Planetary Science Letters* **307**(3), 487-500.

Scholz, C.H., 2019, *The Mechanics of Earthquakes and Faulting*, 2nd ed., 471pp., Cambridge Univ. Press, New York.

Schwartz, D.P., Coppersmith, K.J. 1984. Fault behavior and characteristic earthquakes: Examples from the Wasatch and San Andreas Fault Zones. *Journal of Geophysical Research: Solid Earth* **89**(B7), 5,681-5,698.

Shimazaki, K., Nakata, T., 1980. Time-predictable recurrence model for large earthquakes. *Geophys. Res. Lett.* **7**(4), 279–282.

Sieh, K.E., 1978. Slip along the San Andreas fault associated with the great 1857 earthquake. *Bull. Seismol. Soc. Am.* **68**(5), 1,421–1,448.

Sieh, K.E., Stuiver, M., Brillinger, D., 1989. A more precise chronology of earthquakes produces by the San Andreas Fault in Southern California. *J. Geophys. Res.* **94**, 603–623.

Sieh, K.E., 1996. The repetition of large-earthquake ruptures. *Proc. Natl. Acad. Sci. U.S.A.* **93**, 3,764-3,771.

Stahl, T. and Tye, A., 2020. Schmidt hammer and terrestrial laser scanning (TLS) used to detect single-event displacements on the Pleasant Valley fault (Nevada, USA). *Earth Surf. Proc. Landf.* **45**, 473-483.

Tesson, J., & Benedetti, L., 2019. Seismic history from in situ 36Cl cosmogenic nuclide data on limestone fault scarps using Bayesian reversible jump Markov chain Monte Carlo. *Quaternary Geochronology* **52**, 1-20.

Thingbaijam, K. K. S., Martin Mai, P., Goda, K., 2017. New empirical earthquake source-scaling laws. *Bull. Seismol. Soc. Am.* **107**(5), 2,225-2,246.

Triggs, W., McLauchlan, P., Hartley, R., Fitzgibbon, A., 1999. Bundle Adjustment: A mondern synthesis, in *Vision Algorithms: Theory and Practice*. Springer-Verlag, Corfu, Greece. 298-373.

Tye, A. and Stahl, T. 2018. Field estimate of paleoseismic slip on a normal fault using the Schmidt hammer and terrestrial LiDAR: Methods and application to the Hebgen fault (Montana, USA). *Earth Surf. Proc. Landf.* **43**, 2,397-2,408.

Vai, F., Martini I.P., 2013. Anatomy of an orogen: the Apennines and adjacent Mediterranean basins, Springer Verlag.

Wallace, R.E., 1968. Notes on stream channels offset by the San Andreas Fault, Southern Coast Ranges, California. In: Dickson, W.R., Grantz, A. (Eds.), *Prof. of Conf. on Geologic Problems of the San Andreas fault system*. Stanford Univ. Publ., Geol. Sci., Univ. Ser. 11, pp. 6–21.

Wei, Z., He, H., Shi, F., 2013. Weathering history of an exposed bedrock fault scarp interpreted from its topography. *J. Struct. Geol.* **56**, 34-44. http://dx.doi.org/10.1016/j.jsg.2013.08.008.

Weldon, R.J., Fumal, T., Biasi, G., 2004. Wrightwood and the earthquake cycle. *Geol. Soc. Am. Today* **14**(9). http://dx.doi.org/10.1130/1052-5173.

Wiatr, T., Papanikolaou, I., Fernández-Steeger, T., Reicherter, K., 2015. Bedrock fault scarp history: insight from t-lidar backscatter behavior and analysis of structure changes. *Geomorphology* **228**, 421-431.

737 Youngs, R.R., Coppersmith, K.J., 1985. Implications of fault slip rates and earthquake
738 recurrence models to probabilistic seismic hazard estimates. *Bull. Seismol. Soc. Am.* **75**(4),
739 939–964.
740
741 Zielke, O., Arrowsmith, J.R., 2008. Depth variation of coseismic stress drop explains bimodal
742 earthquake magnitude–frequency distribution. *Geophys. Res. Lett.* **35**, L24301.
743 http://dx.doi.org/10.1029/2008GL036249.
744
745 Zielke, O., Strecker, M.R., 2009. Recurrence of large earthquakes in magmatic continental
746 rifts: insights from a paleoseismic study along the Laikipia-Maramanet fault, Subukia Valley,
747 Kenya Rift. *Bull. Seismol. Soc. Am.* **99**(1), 61-70. http://dx.doi.org/10.1785/0120080015.
748
749 Zielke, O., Arrowsmith, J.R., Ludwig, L.G., Akçiz, S.O., 2010. Slip in the 1857 and Earlier
750 Large Earthquakes Along the Carrizo Plain, San Andreas Fault. *Science* **327**, 1,119-1,122.
751 http://dx.doi.org/10.1126/science.1182781.
752
753 Zielke, O., Klinger, Y., Arrowsmith, J.R., 2015. Fault slip and earthquake recurrence along
754 strike-slip faults — Contributions of high-resolution geomorphic data. *Tectonophysics* **638**, 43-
755 62. http://dx.doi.org/10.1916/j.tecto.2014.11.004.
756
757 Zou, J., He, H., Yokoyama, Y., Shirahama, Y., Sproson, A.D., Wei, Z., Shi, F., Hao, H.,
758 Miyairi, Y., Lü, L., Su, P., Zhou, C., 2020. Seismic history of a bedrock fault scarp using
759 quantitative morphology together with multiple dating methods: A case study of the
760 Luoyunshan piedmont fault, southwestern Shanxi Rift, China. *Tectonophysics* **788**, L228473.
761 http://dx.doi.org/10.1016/j.tecto.2020.228473.